GEOPHYSICS, VOL. 71, NO. 1 (JANUARY-FEBRUARY 2006); P. U13–U20, 10 FIGS.
10.1190/1.2168012

Stability analysis of velocity imaging of 2D multilayered structures through inverse reflected rays

Tan K. Wang[1]

ABSTRACT

Inverse reflected rays are used to image velocities and interfaces in 2D multilayered media. Their direction cosines are specified from the receiver and the source, related respectively to the traveltime gradients of the common-source and common-receiver gathers. Based on the geometry of an inverse ray through the lowest layer, the velocity near the reflection point is derived from either an exact solution or a transcendental equation. For the transcendental equation, the velocity bounds and the imaging stability depend on the interface dips, and the incident angles upon the interface above the reflection point. The velocity imaging is stable or quasi-stable when the reflection point is located between the intersections of the inverse rays and the upper interface.

Application of the technique to a discontinuous normal fault and a forearc basin show that most of the velocity imaging is stable. However, if the inverse reflected rays pass through steep interfaces, the fault plane or highly inhomogeneous media, the imaging is usually unstable because multivalued and incorrect velocities are generated. I conclude that the method is fast and capable of imaging seismic sections with poor quality when compared with prestack depth migration and reflection tomography.

INTRODUCTION

Seismic imaging of the geologically complex structures has advanced from poststack to prestack processing over the past few decades. Most reflected and diffracted arrivals recorded in multichannel seismic data are used now to image velocity structure and interfaces. Prestack depth migration (e.g., Schultz and Sherwood, 1980; Bleistein, 1987; Operto et al., 2000) and migration velocity analysis (e.g., Al-Yahya, 1989; Symes and Carazzone, 1991; Liu, 1997; Wang and Pann, 1998; Woodward et al., 1998; Chauris et al., 2002) most commonly are used to image complex structures such as steep faults, salt domes, and gas sags. To reduce the intensive computation required for prestack depth migration, Hua and McMechan (2003) proposed a limited migration aperture along an inverse ray propagating with an emitted angle of transmission at the source, an emergent angle at a receiver, and intersecting at the reflection point. Both emitted and emergent angles are evaluated from the slopes of the traveltime curves in the common-source and common-receiver gathers. Alternatively, traveltime inversion of the velocity-interface structures is also used in reflection tomography (Bishop et al., 1985; Guiziou et al., 1996). Similar to the enhancement of the prestack depth migration using inverse rays, the traveltimes and their gradients acquired within common-source and common-receiver gathers of reflection tomography (Riabinkin, 1957; Sword, 1986; Billette and Lambaré, 1998; Billette et al., 2003; Wang et al., 2003) are used to rapidly converge upon a velocity model.

The purpose of this paper is to improve the inverse-ray method for seismic imaging of complex structures. Wang (2002) proposed prestack imaging of a 2D homogeneous layer by considering ray geometry and the elliptical envelope generated from a common-source gather, a common-midpoint gather, or a common-offset gather. On the other hand, the layered velocity can be imaged from reflected arrivals based on the emitting and emergent angles of the reciprocal raypath calculated from the traveltime slopes of the common-source and common-receiver gathers (Glogovsky et al., 2002; Wang, 2004). The objective of this paper is to demonstrate an efficient algorithm for using inverse rays to image structural velocities and interfaces in 2D multilayered media, and to test its stability over a range of layer velocity contrasts. I apply the algorithm to a model with a discontinuous normal fault (McClay, 1995) and to a real dataset across a Ryukyu forearc basin.

Manuscript received by the Editor May 27, 2004; revised manuscript received May 29, 2005; published online January 12, 2006.
[1]National Taiwan Ocean University, Institute of Applied Geosciences, No 2, Pei-Ning Road, Keelung 20224, Taiwan. E-mail: tkwang@mail.ntou.edu.tw.

RAY THEORY

In this method, the inverse ray reflected at an interface is traced simultaneously from both the receiver and the source until it merges at the reflection point (Riabinkin, 1957). The direction cosine to the receiver is determined from the traveltime slope of a common-source acquisition (S_2, R_1 and R_2 in Figure 1) and the velocity near the receiver (V_R) so that

$$\cos(\angle R) = -V_R \frac{\Delta t_S}{\Delta x_R}. \tag{1}$$

The direction cosine to the source can be evaluated from the traveltime slope of a common-receiver acquisition (R_1, S_1 and S_2 in Figure 1) and the velocity near the source (V_S) so that

$$\cos(\angle S) = -V_S \frac{\Delta t_R}{\Delta x_S}. \tag{2}$$

The quantities x_R and x_S are the coordinates of the receiver and the source, respectively. The quantities t_R and t_S are the traveltimes from the common-receiver and common-source gathers, respectively. Equation 1 is derived by considering that all rays have equal traveltimes along a wavefront propagating from a common source (S_2 in Figure 1), but along a flat surface there will be traveltime differences between neighboring rays (Wang and Tan, 2003). Thus, the direction of an inverse ray entering a receiver ($\angle R$) is determined from the propagation velocity (V_R), the traveltime difference (Δt_S), and the receiver interval (Δx_R) at the surface. Equation 2 can be derived similarly.

For simplicity, I have assumed that the interface above the reflection point (M, Figure 1) and the velocity above this interface are known, so that I shall image only the velocity below this interface (V_M, Figure 1) and the reflection point by using the inverse rays. This assumption is not necessary if the number of inverse rays reflected at the upper interfaces is sufficient to image the velocity and interface in a layer-stripping manner. However, if the picked traveltimes reflected at the upper interfaces are limited, either the unconstrained structures are interpolated, or the upper model is constrained by other methods. In the following, I investigate the ray geometry, determine the velocity near the reflection point, and analyze the stability of the velocity imaging.

Let the angles at which rays are transmitted through the left and the right sides of any interface above the reflection point (M) in the lowest layer be denoted by θ_L and θ_R, respectively (Figure 2). One of the transmitted angles indicates the direction of a ray propagating from a receiver and another is associated with a source. These transmitted angles are related to the corresponding angles (θ_L and θ_R) of the rays incident upon the left and the right sides of the interfaces, respectively, and are found from Snell's law such that

$$\sin\theta_L = R_V \sin\theta_L \tag{3a}$$

and

$$\sin\theta_R = R_V \sin\theta_R, \tag{3b}$$

where $R_V = V_{k+1}/V_k$ is the velocity ratio between the lower and upper layers. For the case of critical or postcritical incidence ($|\theta_L|, |\theta_R| \geq \theta_{cr}$), the transmitted angles are set equal to $\pm\pi/2$, with the signs depending on the incident angles. If the velocity and the geometry of the interfaces of the upper layers are known, the angles (θ_L and θ_R) of the rays incident upon the interface just above the reflection point can be evaluated by considering rays emitted from a common-receiver gather and a common-source gather (Billette and Lambaré, 1998). However, the velocity ratio R_V is required before determining the transmitted angles.

Based on the sine theorem, an additional equation for constraining R_V is proposed for the ray geometry in Figure 2 such

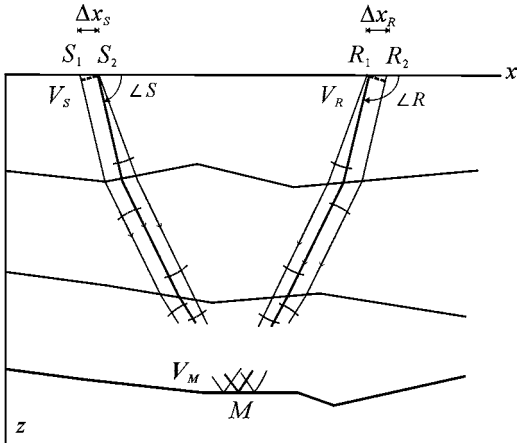

Figure 1. An inverse ray (thick line) emitted from a receiver (R_1) with a direction angle of $\angle R$, shooting from a source (S_2) with a direction angle of $\angle S$, and intersecting at a reflection point (M). The dashed lines indicate the wavefronts propagating from either the common shot (S_2) or the common receiver (R_1). The quantities Δx_S and Δx_R are the shot and receiver intervals, respectively. V_S, V_R, and V_M denote the velocities near the source (S_2), the receiver (R_1) and the reflection point (M), respectively.

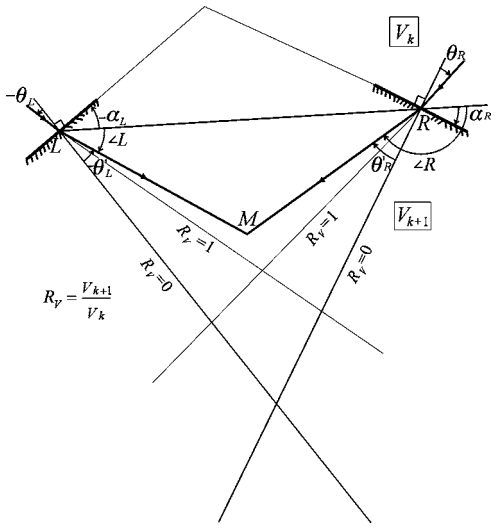

Figure 2. The geometry of a reflected ray (LMR) below the left and right interfaces with dipping angles of α_L and α_R, respectively. The incident and transmitted angles at the left (right) interfaces are denoted by θ_L (θ_R) and θ_L (θ_R), respectively. The rays below LMR denote the special cases of $R_V = 0, 1$.

that

$$\frac{\overline{LM}}{\sin(\angle R)} = \frac{\overline{MR}}{\sin(\angle L)} = \frac{\overline{LR}}{\sin(\angle R - \angle L)} \tag{4a}$$

and

$$\overline{LM} + \overline{MR} = V_{k+1}\delta t, \tag{4b}$$

where the over bar denotes distance between the indicated points. The quantity δt is the traveltime for $\overline{LMR}$ and can be evaluated by subtracting the reflection time from the traveltimes of the raypaths above the line $\overline{LR}$. Equations 4a and 4b then lead to

$$R_V = T\frac{\sin(\angle R) + \sin(\angle L)}{\sin(\angle R - \angle L)} \tag{5a}$$

and

$$T = \overline{LR}/(V_k\delta t). \tag{5b}$$

These quantities can be further reduced by considering that

$$\angle L = \frac{\pi}{2} + \alpha_L + \theta'_L \tag{6a}$$

and

$$\angle R = \frac{\pi}{2} + \alpha_R + \theta'_R, \tag{6b}$$

where α_L and α_R are, respectively, the dipping angles of the left and the right sides of any interface with respect to the vector $\overrightarrow{LR}$. For consistency, the incident angles θ_L, θ_R, and the dipping angles of interfaces α_L and α_R are set between $\pm\pi/2$ with the positive sign indicating clockwise angles and the negative sign associated with counterclockwise angles. The geometry of the reflected ray (LMR) shown in Figure 2 is based on the case of $R_V > 1$, but the special cases of $R_V = 0$ or 1 are also indicated in the figure.

The special case of $\alpha_L = \alpha_R = 0$ for deriving an exact solution of R_V is investigated in Appendix A. For the general case of $\alpha_L \neq 0$ and $\alpha_R \neq 0$, equations 5 provides a transcendental equation for the velocity error such that

$$Verr(R_V) = T\frac{\sin(\angle R) + \sin(\angle L)}{\sin(\angle R - \angle L)} - R_V, \tag{7}$$

where $\angle L$ and $\angle R$ are in terms of θ'_L and θ'_R as shown in equations 6, and angles θ'_L and θ'_R are associated with the Snell's law (3).

The velocity ratio R_V is one of its roots. The derivative of the velocity error is obtained from equations 3, 6, and 7, such that

$$\frac{dVerr(R_V)}{dR_V} = T\frac{1 + \cos(\angle R - \angle L)}{XY\sin^2(\angle R - \angle L)}[Y\sin\theta_L\sin(\angle R) - X\sin\theta_R\sin(\angle L)] - 1, \tag{8}$$

where $X = \sqrt{1 - R_V^2\sin^2\theta_L}$ and $Y = \sqrt{1 - R_V^2\sin^2\theta_R}$. For postcritical incidence, X or Y is set to zero when $R_V|\sin\theta_L| > 1$ or $R_V|\sin\theta_R| > 1$, respectively. A numerical scheme combining the bisection and the Newton-Raphson methods (Press et al., 1992), which considers both equations 7 and 8, is used to solve for R_V. However, before determining R_V, the range and the stability of the possible solutions are investigated.

STABILITY ANALYSIS

I consider four main regions I–IV (Figure 3), depending on the signs of the incident angles θ_L and θ_R, and at least two subregions, based on $R_V > 1$ or $R_V < 1$ within each of these main regions, for analyzing the stability of velocity imaging. Although the reflection point M is located in one of the main regions for a given pair of incident angles, the subregions do not necessarily exist. These main regions can be defined by the rays passing through L and R when $R_V = 0$ or $R_V = 1$. The direction angles of these rays measured clockwise from $\overrightarrow{LR}$ are $\pi/2 + \alpha_L$ and $\pi/2 + \alpha_L + \theta_L$ (or $\pi/2 + \alpha_R$ and $\pi/2 + \alpha_R + \theta_R$) when $R_V = 0$ and $R_V = 1$, respectively.

In the following, I specify the main regions and their subregions of Figure 3, describe the lower bound (R_{V1}) and the upper bound (R_{V2}) of velocity in the subregions, and investigate the stability of velocity imaging.

Region I: $\theta_L < 0$ and $\theta_R > 0$

Subregion I-1a. $\alpha_L < 0$ and $\alpha_R > 0$

This subregion lies above $\overline{LR}$ with the lower and upper bounds of imaging velocities near $\overline{LR}$ and at the top of the subregion as specified in Figure 3, respectively. Since the transmitted angle of an inverse ray along $\overline{LR}$ (dashed line in Figure 3) from the left is $-(\pi/2 + \alpha_L)$, the velocity ratio $R_V = -\cos\alpha_L/\sin\theta_L$, according to equation 3. Similarly, if an inverse ray propagates along $\overline{LR}$ from the right, its transmitted angle

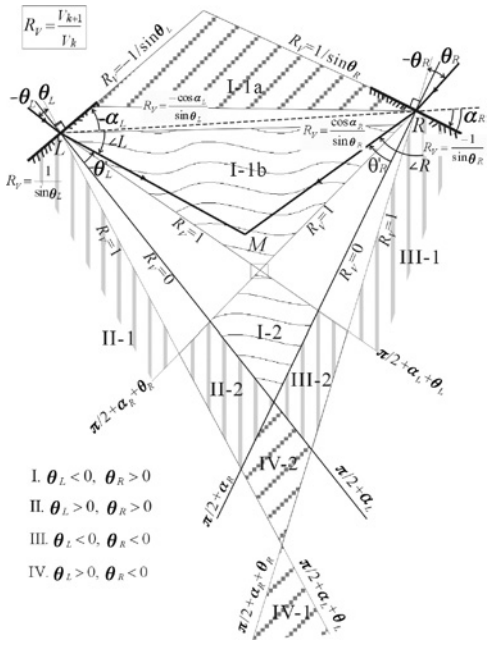

Figure 3. Range and stability analysis of velocity imaging through reflected rays when $-\cos\alpha_L/\sin\theta_L > \cos\alpha_R/\sin\theta_R$. Velocity imaging is unique and stable in subregions I-1b and I-2 (curved shading) whereas it is quasi-stable in subregions I-1a, IV-1, and IV-2 (inclined shading). Subregions II-1, II-2, III-1, and III-2 (vertical shading) possess multiple and unstable solutions for velocity imaging. The angles labeled at the end of lines are measured clockwise from the vector $\overrightarrow{LR}$ (dashed line).

is $\pi/2$–α_R, and the velocity ratio $R_V = \cos\alpha_R/\sin\theta_R$. However, since the velocity ratio of the inverse ray along $\overline{LR}$ from the left is not necessarily equal to that from the right, the inverse ray propagating along $\overline{LR}$ does not necessarily exist. For example, if the velocity ratio $-\cos\alpha_L/\sin\theta_L > \cos\alpha_R/\sin\theta_R$ (as shown in Figure 3), an inverse ray with the velocity ratio of $\cos\alpha_L/\sin\theta_L$ can propagate along $\overline{LR}$ from the left but transmits above $\overline{LR}$ from the right, as denoted by the lower boundary of region I-1a in Figure 3. Therefore, the lower bound of the velocity ratio is determined by

$$R_{V1} = \max\left(-\frac{\cos\alpha_L}{\sin\theta_L}, \frac{\cos\alpha_R}{\sin\theta_R}\right). \tag{9}$$

On the other hand, since the top of this subregion is the extension of the left and the right sides of the interfaces, the upper bound of the velocity ratio is determined by

$$R_{V2} = \max\left(-\frac{1}{\sin\theta_L}, \frac{1}{\sin\theta_R}\right). \tag{10}$$

The maximum value in equation 10 is due to the possibility of postcritical incidence in which the velocity ratio $-1/\sin\theta_L$ or $1/\sin\theta_R$ is underestimated. Furthermore, since the ray distance is increasing when R_V increases in this subregion, the calculated velocity ratio $R_V^* = T\frac{\sin(\angle R)+\sin(\angle L)}{\sin(\angle R-\angle L)}$ is increasing also, which can be confirmed from equation 8 since $\sin\theta_L \sin\angle R > 0$ and $\sin\theta_R \sin\angle L < 0$. The increasing nature of the calculated velocity ratio R_V^* implies that the velocity imaging in this subregion is quasi-stable.

Subregion I-1b $\alpha_L + \theta_L > -\pi/2$, $\alpha_R + \theta_R < \pi/2$, and $R_{V1} = 1$

This subregion is below $\overline{LR}$, but the extension of either the left or right side of the interface can be either above $\overline{LR}$ if $\alpha_L < 0$ (or $\alpha_R > 0$) or below $\overline{LR}$ if $\alpha_L \geq 0$ (or $\alpha_R \leq 0$). Therefore, the upper bound of the velocity ratio in this subregion depends on the signs of α_L and α_R such that

$$R_{V2} = \min\left(-\frac{\cos\alpha_L}{\sin\theta_L}, \frac{\cos\alpha_R}{\sin\theta_R}\right), \tag{11}$$

for $\alpha_L < 0$ and $\alpha_R > 0$;

$$R_{V2} = \max\left(-\frac{1}{\sin\theta_L}, \frac{1}{\sin\theta_R}\right), \tag{12}$$

for $\alpha_L \geq 0$ and $\alpha_R \leq 0$;

$$R_{V2} = \max\left(-\frac{\cos\alpha_L}{\sin\theta_L}, \frac{1}{\sin\theta_R}\right), \tag{13}$$

for $\alpha_L < 0$ and $\alpha_R \leq 0$; and

$$R_{V2} = \max\left(-\frac{1}{\sin\theta_L}, \frac{\cos\alpha_R}{\sin\theta_R}\right), \tag{14}$$

for $\alpha_L \geq 0$ and $\alpha_R > 0$. As in equation 10, the maximum values in equations 11–14 are created by the possibility of postcritical incidence. Since the ray distance is decreasing when R_V increases (or when $\sin\theta_L \sin\angle R < 0$ and $\sin\theta_R \sin\angle L > 0$ in equation 8), the calculated velocity ratio $R_V^* = T\frac{\sin(\angle R)+\sin(\angle L)}{\sin(\angle R-\angle L)}$ is decreasing. Therefore, velocity imaging in this subregion is stable, and a unique solution can be obtained when $Verr(R_{V1} = 1) \geq 0$ and $Verr(R_{V2}) \leq 0$.

Subregion I-2. $\alpha_L + \theta_L < \alpha_R + \theta_R$, $R_{V1} = 0$ and $R_{V2} = 1$

This subregion exists if rays with direction angles of $\pi/2 + \alpha_L + \theta_L$ and $\pi/2 + \alpha_R + \theta_R$ ($R_V = 1$) intersect (Figure 3). As in Subregion I-1b, the calculated velocity ratio R_V^* decreases when R_V increases. Therefore, velocity imaging in this subregion is stable and unique provided that $Verr(1) \leq 0$.

Region II: $\theta_L > 0$ and $\theta_R > 0$

Subregion II-1. $\alpha_R + \theta_R < \pi/2$, and $R_{V1} = 1$

This subregion is enclosed by the left interface and by rays with direction angles of $\pi/2 + \alpha_L + \theta_L$ and $\pi/2 + \alpha_R + \theta_R$. However, its existence depends only on the ray emitted from R when $R_V = 1$. Furthermore, the upper bound of the velocity ratio is

$$R_{V2} = \max\left(\frac{1}{\sin\theta_L}, \frac{\cos\alpha_R}{\sin\theta_R}\right) \tag{15}$$

because it is constrained by the left interface for the ray emitted from L and by the vector $\overleftarrow{LR}$ for the ray from R. The possibility of postcritical incidence has been considered in equation 15.

Subregion II-2. $\alpha_R + \theta_R > \alpha_L$, $R_{V1} = 0$ and $R_{V2} = 1$

If this subregion exists, it is below the lines of $\pi/2 + \alpha_L$ and $\pi/2 + \alpha_R + \theta_R$.

Region III: $\theta_L < 0$ and $\theta_R < 0$

Subregion III-1. $\alpha_L + \theta_L > -\pi/2$, and $R_{V1} = 1$

This region is similar to Subregion II-1. Its existence depends only on the ray emitted from L when $R_V = 1$. Since the maximum velocity imaged in this region is determined from either the vector $\overrightarrow{LR}$ for the ray emitted from L or the right interface for the ray emitted from R, the upper bound of the velocity ratio is

$$R_{V2} = \max\left(-\frac{\cos\alpha_L}{\sin\theta_L}, -\frac{1}{\sin\theta_R}\right), \tag{16}$$

in which postcritical incidence is considered.

Subregion III-2. $\alpha_L + \theta_L < \alpha_R$, $R_{V1} = 0$ and $R_{V2} = 1$

If this subregion exists, it is below the lines of $\pi/2 + \alpha_L + \theta_L$ and $\pi/2 + \alpha_R$.

Region IV: $\theta_L > 0$ and $\theta_R < 0$

Subregion IV-1. $\alpha_L + \theta_L < \alpha_R + \theta_R$, and $R_{V1} = 1$

If this subregion exists, it is below the lines of $\pi/2 + \alpha_L + \theta_L$ and $\pi/2 + \alpha_R + \theta_R$. The upper bound of its velocity ratio is

$$R_{V2} = \max\left(\frac{1}{\sin\theta_L}, -\frac{1}{\sin\theta_R}\right), \tag{17}$$

because it is constrained by the left and right interfaces with the possibility of postcritical incidence.

Subregion IV-2. $\alpha_L < \alpha_R$, $R_{V1} = 0$ and $R_{V2} = 1$

If this subregion exists, it is below the lines of $\pi/2 + \alpha_L$ and $\pi/2 + \alpha_R$.

In summary, velocity imaging in regions II and III is unstable and nonunique because the calculated velocity ratio R_V^* does not monotonically increase or decrease. Because the ray distance in region IV is increasing when R_V increases (or $\sin\theta_L \sin\angle R > 0$ and $\sin\theta_R \sin\angle L < 0$ in equation 8), the calculated velocity ratio R_V^* is increasing. Therefore, similar to Subregion I-1a, velocity imaging in region IV is quasi-stable.

APPLICATION TO A DISCONTINUOUS NORMAL FAULT

Velocity imaging through inverse reflected rays is now applied to a discontinuous normal fault with 11 layers and increasing P-wave velocity of 1.8–3.6 km/s (McClay, 1995). The synthetic traveltimes (Figure 4) are calculated based on a marine-seismic acquisition that included 20 shots, which started at distance of 2 km, ended at 11.5 km, and had a uniform shot interval of 0.5 km. A total of 100 hydrophones were used with a near offset of 0.2 km and a receiver interval of 0.05 km.

For display, I select rays for only one tenth of the receivers to image the uppermost layer based on the traveltime curve fitting (Wang, 2002). However, I consider all receivers for constructing the lowest inverse rays in the rest of the layers (Figure 5). Most of the layer velocities (Figure 6) are determined accurately from the exact solution (red rays in Figure 5). Furthermore, the velocity imaging is unique and stable in Subregion I-1b where the reflection point is located between the transmitted points of rays at the upper interface, as shown by blue rays in Figure 5. However, within subregions II-1 and III-1, velocity imaging based on rays reflected from steep interfaces is unstable (green and yellow rays in Figure 5) because they generate accurate (colored rays in Figure 6) and inaccurate velocities (black rays in Figure 6). The velocity imaged from subregions II-1 and III-1 is most inaccurate in the third layer of the discontinuous normal fault. Fortunately, large velocity errors are readily detectable based on the stability analysis proposed in this study.

In order to distinguish the accurate velocity from the quasi-stable and unstable solutions such as those in regions I-1a, II, III, and IV (Figure 3), I use the coherence of velocity imaging along horizons if the lateral velocity varies smoothly between neighboring inverse rays. For example, in the case of the discontinuous normal fault, all inaccurate velocities (black rays in Figure 6) can be identified except those near the fault or at the steep interface (yellow rays in Figure 5).

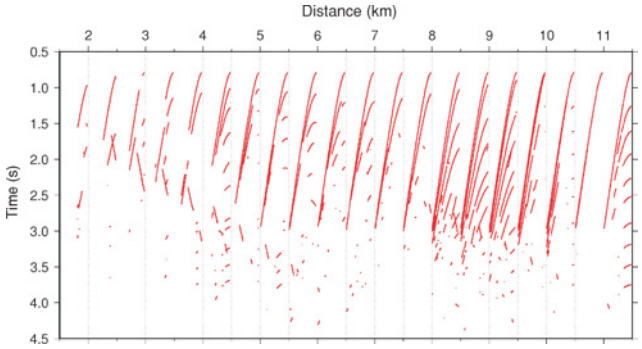

Figure 4. Picked reflected arrivals of twenty common-shot gathers simulated from a discontinuous normal model. The near and far offsets of the common-shot gathers are 0.2 km and 5.15 km, respectively.

APPLICATION TO A RYUKYU FOREARC BASIN

Oblique subduction of the Philippine Sea Plate (PSP) and collision of the Luzon Arc off eastern Taiwan (inset of Figure 7) have generated high seismicity and resulted in the complex crustal structures near the northwestern edge of the southernmost Ryukyu forearc region (Figure 7). The shallow and strong earthquakes below the Nanao Basin are more frequent than those below other forearc basins.

I used reflection data collected along a seismic line (Figure 7) parallel to the arc to image the sedimentary structure of the Nanao Basin and to investigate the high seismicity below the basin. Fourteen shot records with 156 receivers, a shot interval of about 50 m, and a receiver interval of 25 m (Figure 8) are selected from the data set to demonstrate the capability of inverse-ray imaging. The reflected traveltimes over

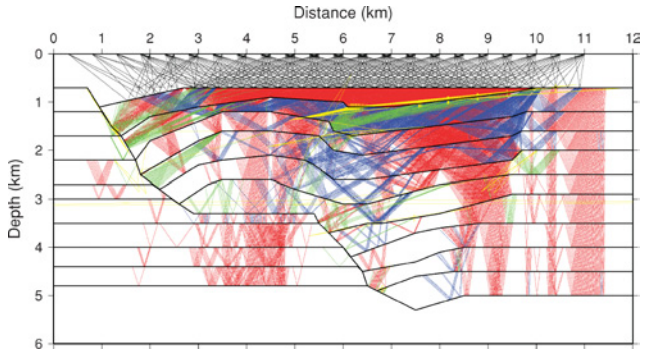

Figure 5. Inverse reflected rays through all layers of the discontinuous normal model. Black rays result from velocity imaging of the uppermost layer through fitting traveltime hyperbolas (Wang, 2002). Red, blue, green, and yellow rays are associated with the exact, stable, unstable, and multiple solutions of the velocity imaging, respectively. Black rays with cross marks and all yellow rays show incorrect imaging of reflection points.

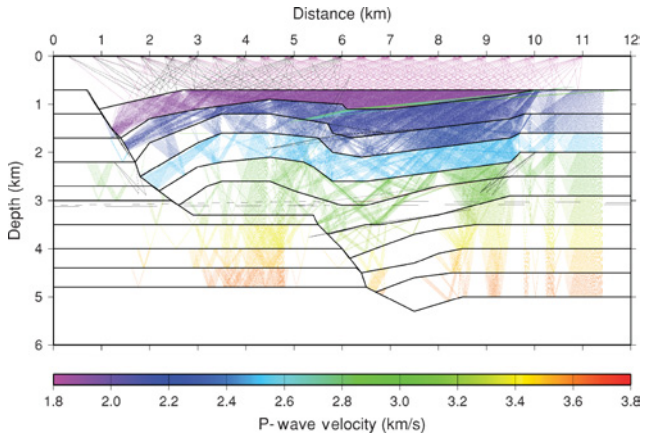

Figure 6. Imaging of layer velocities of the discontinuous normal model through inverse reflected rays. Colors of the rays denote the imaging velocity. The black rays indicate the incorrect velocities imaged from the multiple solutions.

the shallower section (two-way time less than 6 s) of the basin are easily picked and nearly the same at all offsets. Those associated with the deeper section (between distances of about 36–46 km) show dipping interfaces with strong amplitude contrasts and a maximum arrival time of about 9 s (Figure 8). Following equation 1, I used traveltime slopes of the shot records (picked from Figure 8) and the P-wave velocity of seawater (1.5 km/s) to determine the direction of inverse rays emitted from receivers. However, in view of equation 2, I had to sort the data set into common-receiver gathers to evaluate the direction of inverse rays shooting from sources.

By considering fourteen shot records and their common-receiver gathers, layer-stripping and inverse-ray imaging of the Nanao Basin show that most of the layer velocities and interfaces imaged by the exact solution (Appendix A) are also imaged by the inverse-ray method (Figure 9a). The numerical solutions (Figure 9b), which include stable, quasi-stable, and unstable solutions, provide a good image of the deep and steep layers except in the high velocity (> 5 km/s) zone below the basin where multivalue solutions (red, dashed lines) exist.

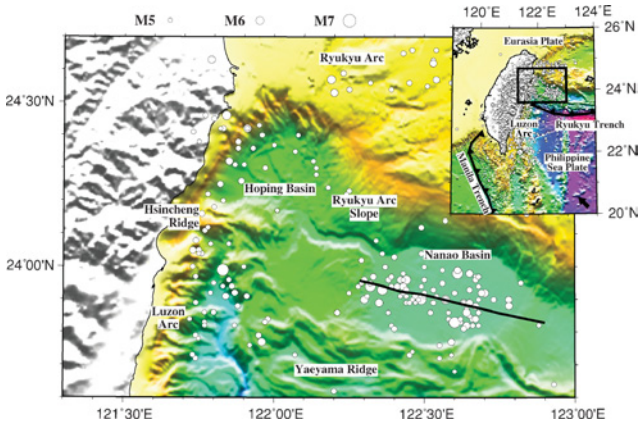

Figure 7. Bathymetry (shaded relief) and epicenters (open circles) off eastern Taiwan in the southernmost Ryukyu forearc region. The bathymetry is plotted from a digital elevation model (Liu et al., 1998). The epicenters for magnitudes greater than five and focal depth less than 40 km are plotted from data courtesy of the Central Weather Bureau of Taiwan. A seismic line across the Nanao Basin, with an average shot interval of about 50 m, is considered for inverse-ray imaging.

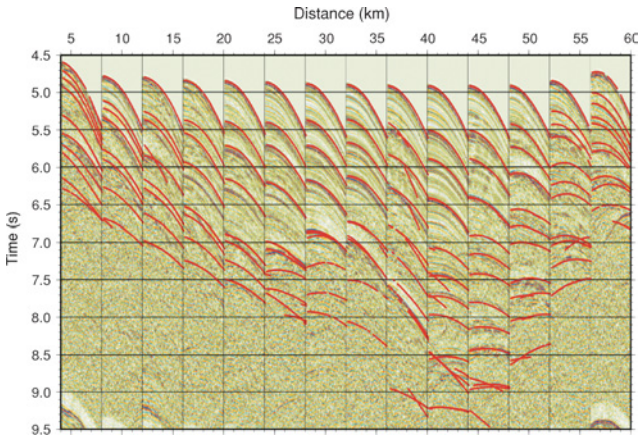

Figure 8. Selective shot records and picked arrivals along the seismic line across the Nanao Basin shown in Figure 7. The near offset and the receiver interval of the 156-hydrophone streamer are 200 m and 25 m, respectively.

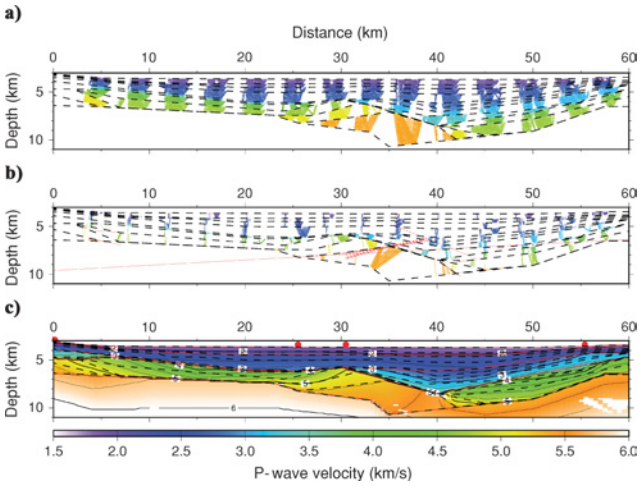

Figure 9. (a) Exact and (b) numerical solutions of inverse-ray imaging of the Nanao Basin. Only inverse reflected rays resulting from the selective shot records of Figure 8 are shown. The colors of the rays denote the imaging velocity, and the red dashed lines indicate incorrect solutions. The velocity model of the Nanao Basin (c) is derived from traveltime inversion of reflection and refraction data (Wang et al., 2004) recorded by four ocean-bottom seismometers (red solid circles). Reflection interfaces imaged by inverse rays (dashed lines) are superimposed on the velocity model. Color code in (a), (b), and (c) is the same.

To confirm imaging of the Nanao Basin through inverse rays, a velocity model (Figure 9c) inverted from reflection and refraction traveltimes along the same line (Wang et al, 2004) is given for comparison. Both results are generally consistent except at the Ryukyu Arc Basement (velocity > 4 km/s) where the assumption of the homogeneous layer is no longer valid because of the large velocity gradient. Two kinds of velocity anomalies are found here. The first is the velocity (4–5 km/s) undulation beneath the Nanao Basin, which I attribute to subducted/underplated sediment scraped from the downgoing oceanic plate. The second is the high-velocity (> 5 km/s) zone that has resulted from the arc-parallel compression caused by the oblique subduction of the PSP (Wang et al., 2004). These velocity anomalies also support the high seismicity below the Nanao Basin.

CONCLUSION

Reflected arrivals and their spatial derivatives of a common-source gather and a common-receiver gather have been used to image the velocity-interface structure in the lowest layer of the inverse rays. An exact solution of the velocity near the reflection point has been presented where an interface, through which an inverse ray has been transmitted downward from a source and a receiver, above the reflection point is smooth. For the general case of the velocity imaging near the reflection point, the stable, quasi-stable and unstable solutions, depending on the incident angles of an inverse ray through the upper

interface and the interface dips, are proposed also. The lower and upper bounds of the velocity are clearly specified for each kind of the numerical solution solved by the bisection and the Newton-Raphson methods.

The inverse-ray method presented here is capable of rapid computation and of imaging seismic sections with poor quality; whereas, prestack depth-migration and reflection tomography usually require much more computational time. However, the uncertainty in picking traveltimes and calculating their spatial derivatives are the main limitations of inverse-ray imaging. In particular, velocity imaging is very sensitive to the slope of the traveltime curve, which can be picked more accurately from the slant stack (Billette and Lambaré, 1998; Billette et al., 2003).

The inverse reflected rays studied here can be applied readily to inverse diffracted rays if diffracted arrivals can be picked from common-source and common-receiver gathers. For the case of the discontinuous normal fault, inverse diffracted rays may propagate through the fault and thus image the most complex structure near it. The inverse-ray method can be applied also to laterally varying media, provided that the lateral velocity varies smoothly. However, for highly inhomogeneous media such as the Ryukyu Arc Basement beneath the Nanao Basin, inverse-ray imaging will be limited near the reflection and diffraction points.

ACKNOWLEDGMENTS

Encouragements and suggestions from reviewers are appreciated. I would like to thank Drs. V. Glogovsky, E. Landa, and J. Paffenholz for providing translated Russian literature. This research was supported by National Science Council, Republic of China through the grant NSC 91-2611-M-019-006 and NSC 92-2611-M-019-015.

APPENDIX A

AN EXACT SOLUTION

I investigate the special case of $\alpha_L = \alpha_R = 0$; i.e., when the left and right sides of the interfaces above the reflection point are along $\overline{LR}$ (Figure A1). This case allows an exact solution

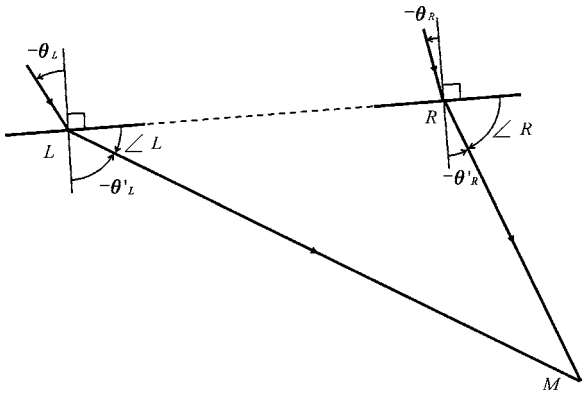

Figure A-1. A special case for deriving an exact solution of the layer velocity. The interface above the reflection point (M) is along $\overline{LR}$ for which $\alpha_L = \alpha_R = 0$.

for R_V. Substituting equations 6 and 3 into equation 5, I obtain

$$R_V \sin(\theta'_R - \theta'_L) = R_V^2(\sin\theta_R \cos\theta'_L - \sin\theta_L \cos\theta'_R)$$
$$= T(\cos\theta'_R + \cos\theta'_L). \quad \text{(A-1)}$$

By considering $\cos\theta'_L = \sqrt{1 - R_V^2 \sin^2\theta_L}$ and $\cos\theta'_R = \sqrt{1 - R_V^2 \sin^2\theta_R}$, equation 5 is reduced to

$$(\sin\theta_R R_V^2 - T)\sqrt{1 - R_V^2 \sin^2\theta_L}$$
$$= (\sin\theta_L R_V^2 + T)\sqrt{1 - R_V^2 \sin^2\theta_R}, \quad \text{(A-2)}$$

where θ_L, θ_R, and T are known. Squaring both sides of equation A-2 and algebraic manipulation lead to the exact solution

$$R_V^2 = \frac{2 - T(\sin\theta_R - \sin\theta_L)}{2T \sin\theta_L \sin\theta_R + \sin\theta_R - \sin\theta_L} T \geq 0. \quad \text{(A-3)}$$

This solution is similar to that for finding the equivalent velocity from the surface to the reflection point proposed by Sword (1987) and Billette et al. (2003). Both the highest order (R_V^6) and the constant term vanish after squaring both sides of equation A-2 so that only R_V^2 are left in the final solution A-3.

REFERENCES

Al-Yahya, K. M., 1989, Velocity analysis by iterative profile migration: Geophysics, **54,** 718–729.
Billette, F., S. L. Begat, P. Podvin, and G. Lambaré, 2003, Practical aspects and applications of 2D stereotomography: Geophysics, **68**, 1008–1021.
Billette, F., and G. Lambaré, 1998, Velocity macro-model estimation from seismic reflection data by stereotomography: Geophysical Journal International, **135**, 671–690.
Bishop, T. N., K. P. Bube, R. T. Cutler, R. T. Langan, P. L. Love, J. R. Resnick, R. T. Shuey, and D. A. Spinder, 1985, Tomographic determination of velocity and depth in laterally varying media: Geophysics, **50**, 903–923.
Bleistein, N., 1987, On the imaging of reflectors in the earth: Geophysics, **52,** 931–942.
Chauris, H., M. Noble, G. Lambaré, and P. Podvin, 2002, Migration velocity analysis from locally coherent events in 2-D laterally heterogeneous media, Parts I and II: Geophysics, **67**, 1202–1224.
Glogovsky, V., E. Landa, and J. Paffenholz, 2002, Integrated approach to subsalt depth imaging: Synthetic case study: The Leading Edge, **21**, 1217–1223.
Guiziou, J. L., J. L. Mallet, and R. Madariaga, 1996, 3-D seismic reflection tomography on top of the GOCAD depth modeler: Geophysics, **61**, 1499–1511.
Hua, B. L., and G. A. McMechan, 2003, Parsimonious 2-D prestack Kirchhoff depth migration: Geophysics, **68**, 1043–1051.
Liu, C. S., S. Y. Liu, S. E. Lallemand, N. Lundberg, and D. L. Reed, 1998, Digital elevation model offshore Taiwan and its tectonic implications: Terrestrial, Atmospheric and Oceanic Sciences, **9**, 705–738.
Liu, Z., 1997, An analytical approach to migration velocity analysis: Geophysics, **62**, 1238–1249.
McClay, K. R., 1995, 2D and 3D analogue modeling of extensional fault structures: Templates for seismic interpretation: Petroleum Geology, **1**, 163–178.
Operto, S., S. Xu, and G. Lambaré, 2000, Can we image quantitatively complex models with rays?: Geophysics, **65**, 1223–1238.
Press, W. H., S. A. Teukolsky, W. T. Vetterling, and B. P. Flannery, 1992, Numerical recipes in C: the art of scientific computing: Cambridge University Press, 362–368.
Riabinkin, L. A., 1994, Fundamentals of resolving power of controlled directional reception (CDR) of seismic waves, in G. H. F. Gardner and L. Lu, eds., Slant Stack Processing: Society Exploration Geophysicists Geophysics Reprint series, **14**, 36–60.
Schultz, P. S., and J. W. C. Sherwood, 1980, Depth migration before stack: Geophysics, **45,** 376–393.

Sword, C. H., 1986, Tomographic determination of interval velocities from picked reflection seismic data: 56th Annual International Meeting, SEG, Expanded Abstracts, 657–660.
Sword, C. H., 1987, Tomographic determination of interval velocities from reflection seismic data: The method of controlled directional reception: Ph.D. dissertation, Stanford University.
Symes, W. W., and J. J. Carazzone, 1991, Velocity inversion by differential semblance optimization: Geophysics, **56,** 654–663.
Wang, B., T. Butkus, H. Zhu, and D. Pham, 2003, Key aspects of 3D reflection traveltime tomography: 73rd Annual International Meeting, SEG, Expanded Abstracts, 646–649.
Wang, B., and K. Pann, 1998, Model-based interpretation of focusing panels for depth focusing analysis: 68th Annual International Meeting, SEG, Expanded Abstracts, 1596–1599.
Wang, T. K., 2002, Prestack inverse-ray imaging of a 2D homogeneous layer: A tutorial study: Terrestrial, Atmospheric and Oceanic Sciences, **13**, 399–416.
Wang, T. K., 2004, Inverse-ray imaging of velocity-interface structures: Application to the southernmost Ryukyu subduction zone: Western Pacific Geophysics Meeting, EOS Transactions of American Geophysical Union, **85**, WP143.
Wang, T. K., S. F. Lin, C. S. Liu, and C. S. Wang, 2004, Crustal structure of the southernmost Ryukyu subduction zone: OBS, MCS and gravity modeling: Geophysical Journal International, **157**, 147–163.
Wang, T. K., and S. C. Tan, 2003, Inverse-ray imaging of 2D layered structures from seismic reflection data: Chinese Journal of Mechanics, Series A, **19**, 191–196.
Woodward, M. J., P. Farmer, D. Nichols, and S. Charles, 1998, Automated 3-D tomographic velocity analysis of residual moveout in prestack depth migrated common image point gathers: 68th Annual International Meeting, SEG, Expanded Abstracts, 1218–1221.